Southern Hemisphere forcing of Pliocene δ^{18}O and the evolution of Indo-Asian monsoons

Steven C. Clemens,[1] Warren L. Prell,[1] Youbin Sun,[2] Zhengyu Liu,[3] and Guangshan Chen[2,3]

[1]   The Milankovitch paradigm links the timing (phase) of ice volume minima to summer insolation maxima in the hemisphere where ice volume dominates; consistent application of this paradigm dictates that Pliocene ice volume minima should lag Southern Hemisphere summer insolation maxima. We infer the magnitude of this lag on the basis of the phase relationship between equatorial sea surface temperature and benthic δ^{18}O. We infer that Pliocene δ^{18}O minima should lag obliquity maxima by 19° (2.2 ka), broadly consistent with the current global marine δ^{18}O chronology, and precession maxima by 32° (2 ka), a difference of 160° (10.2 ka) relative to the current global marine δ^{18}O chronology. Only in the context of this revision are Pliocene summer and winter monsoon phase relationships consistent with direct orbital forcing across the entire Indo-Asian region, including marine and terrestrial proxies from the Chinese Loess Plateau, the South China Sea, and the Arabian Sea. Strong Pliocene summer and winter monsoons were in phase with one another, strengthened at obliquity minima and precession minima; the summer monsoon was also strengthened at precession maxima, yielding a semiprecession spectral signal. Strong Pliocene monsoons at orbital extremes indicate a direct response to fast physics processes including sensible heating and cooling of the Asian landmass and, for the summer monsoon, the export of latent heat from the southern Indian Ocean. As Northern Hemisphere ice volume grew into the Pleistocene, the timing of strong winter and summer monsoons drifted apart becoming influenced by the combined effects of fast physics and slow physics (ice volume) variables. The phase of strong winter monsoons shifted toward ice maxima, and the phase of strong summer monsoons shifted toward ice minima.

1. Introduction

[2]   We analyze fourteen marine and terrestrial monsoon proxy records from three geographic regions including the Arabian Sea (AS), South China Sea (SCS), and Chinese Loess Plateau (CLP) (Figure 1). Our goal is to understand the summer monsoon (SM) and winter monsoon (WM) response to insolation forcing and the evolution of global ice volume, from the Pliocene when Southern Hemisphere (SH) ice sheets dominated, through the Pleistocene when Northern Hemisphere (NH) ice sheets dominated [*Shackleton et al.*, 1984]. To this end, two requirements must be met. First, we must be able to link the timing of changes in marine δ^{18}O to insolation forcing. This is necessary because all the SM and WM proxies, including those from the CLP [*Sun et al.*, 2006], are linked to one another and to insolation forcing through marine δ^{18}O and its associated chronology. Second, we must quantitatively measure the

timing of changes in WM and SM proxies relative to changes in the marine δ^{18}O record (a proxy for global ice volume). This is accomplished using cross-spectral analysis to isolate and quantify the coherence and phase relationships within the Earth-orbital 41 ka (obliquity) and 23 ka (precession) bands. We first address these two issues followed by analysis of the Indo-Asian monsoon proxies, identifying an internally consistent set of evolving phase relationships between proxies of monsoon intensity, orbital-scale solar radiation, and the Plio-Pleistocene evolution of global ice volume.

2. Analytical Approach

[3]   Our approach relies on multiproxy time series analysis in which the common variance among different monsoon-influenced proxies, at specific orbital frequency bands, is interpreted as the common response to monsoon forcing [*Clemens and Prell*, 2003]. This multiproxy frequency-specific approach acknowledges two important facts. First, no proxy currently in use can claim a unique, direct response to a single climate variable; all have the potential to be modified by unrelated chemical, physical, or biological processes. The multiproxy approach attempts to minimize nonmonsoon variance by interpreting the ensemble results of multiple independent proxies from different geographic locations, each linked to monsoon circulation but

---

[1]Department of Geological Sciences, Brown University, Providence, Rhode Island, USA.
[2]Institute of Earth Environment, Chinese Academy of Sciences, Xi'an, China.
[3]Center for Climatic Research, University of Wisconsin, Madison, Wisconsin, USA.
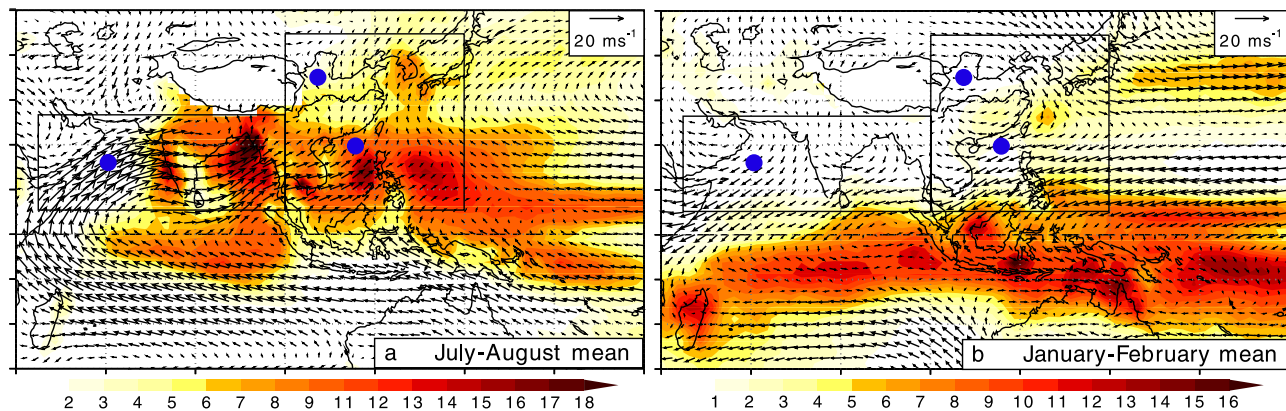
Figure 1. Monsoon winds (arrows; m s^{-1}), precipitation (shading; mm d^{-1}), and site locations (dots). Ocean Drilling Program (ODP) Site 722 in the Arabian Sea (16°37′N, 59°48′E, 2028 m below sea level), ODP Site 1146 in the South China Sea (19°27′N, 116°16′E, 2092 m below sea level), and stacked records from Lingtai (35°04′N, 107°39′E, 1350 m above sea level) and Zhaojiachuan (35°45′N, 107°49′E, 1250 m above sea level) on the south central Chinese Loess Plateau. Boxes delineate the Indian and east Asian monsoon sectors. Climatological (a) summer and (b) winter mean precipitation (CMAP, 1979–2000) and wind patterns (NCEP/NCAR reanalysis, 1951–2000) are after *Wang et al.* [2003].

impacted differently nonmonsoonal processes. For these reasons, we do not necessarily associate long-term changes in the mean of any of the marine proxies with long-term changes in the strength of WM and SM circulation; we interpret only the relative timing (phase) of coherent variance at discrete earth-orbital frequency bands. Second, climate records are mixtures of variance from processes operating at multiple but discrete orbital frequency bands, rendering visual analysis of coherence and phase relationships difficult and, likely, misleading; quantitative means of coherence and phase analysis are crucial.

[4] Cross-spectral analysis is used to quantitatively estimate coherence and phase relationships among climate proxies within three key intervals of time chosen to reflect changes in the mean, amplitude, and phase of CLP [*Sun et al.*, 2006], AS [*Altabet et al.*, 1999; *Clemens et al.*, 1996], and SCS proxies as well as the timing of major changes in benthic δ^{18}O [*Lisiecki and Raymo*, 2007]. The three intervals are: 5 to 2.75 Ma, an interval characterized by dominance of SH ice volume; 2.75 to 1.25 Ma, an interval characterized by rapid growth and dominance of NH ice volume; and 1.25 Ma to present, an interval characterized by high-amplitude ice age cycles. This spectral approach quantifies the timing of SM and WM responses relative to

the evolution of global ice volume; such results are largely independent of the absolute δ^{18}O chronology because they are "within core" analyses. However, understanding the relationship between insolation forcing and monsoon circulation does depend on the absolute δ^{18}O chronology, because δ^{18}O is the common chronostratigraphic link among all monsoon proxies. Hence, a reliable understanding of the timing of ice volume relative to insolation forcing is critical.

3. Phase of δ^{18}O Relative to Insolation Forcing

[5] The phase of δ^{18}O relative to insolation forcing is well established for the younger interval of time, 1.25 Ma to present, where NH ice volume dominates. Here the SPECMAP results linking ice growth and decay to 65°N summer insolation indicates a 17 ka time constant [*Imbrie et al.*, 1984]. This time constant is equivalent to a 78° (5 ka) lag between NH summer insolation maxima and δ^{18}O (ice volume) minima at the precession band and a 69° (7.8 ka) lag at the obliquity band (Table 1). In contrast, the time constants for the two older intervals of time are highly under constrained [*Lisiecki and Raymo*, 2005; *Lisiecki and Raymo*, 2007]. The latest global marine δ^{18}O chronology [*Lisiecki and Raymo*, 2005] employed smaller time con-

Table 1. Time Constant and Phase Relative to Orbital Parameters[a]

	Precession Minima (21 June Perihelion)			Obliquity Maxima		
	0–1.25 Ma	1.25–2.75 Ma	2.75–5.0 Ma	0–1.25 Ma	1.25–2.75 Ma	2.75–5.0 Ma
TC	17 ka	6.5 ka	2.3 ka	17 ka	6.5 ka	2.3 ka
δ^{18}O min	−78°	−60°	−212°	−69°	−44°	−19°
δ^{18}O max	−258°	−240°	−32°	−249°	−224°	−199°
SM max	−127° ± 52°	−142° ± 51°	−4° ± 4°, −203° ± 35°	−46° ± 15°	−33° ± 7°	−216° ± 48°
WM max	−298° ± 9°	−313° ± 27°	−1° ± 14°	−286° ± 35°	−285° ± 74	−139° ± 29°

[a]TC, time constant of the ice sheets; WM max, winter monsoon maxima; SM max, summer monsoon maxima. Negative phases indicate a lag relative to the orbital parameter.
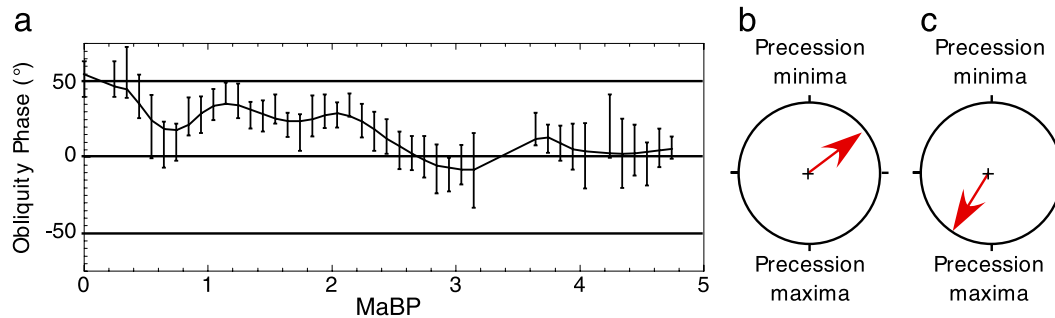
Figure 2. (a) Obliquity band evolutive cross-spectral phase results for alkenone SST maxima relative to ice volume minima in the eastern equatorial Pacific (ODP Site 846) [*Lawrence et al.*, 2006]. Positive values indicate that SST maxima lead ice volume minima. Evolutive cross-spectral analysis uses a 500 ka window with 100 ka time steps beginning at 250 ka. Phase results and associated errors are plotted at the midpoint of each window, provided statistical significance exceeds the 80% CI, and connected using a 20% weighted smooth to emphasize the long-term trend. Bandwidth is 0.00784 ka^{-1}. (b and c) Precession band phase wheels for the oldest interval of time (5 to 2.75 ma). The phase of ice minima (red arrow) in the latest marine $\delta^{18}O$ chronology [*Lisiecki and Raymo*, 2005] lags precession minima by 53° (Figure 2b) whereas in our revised chronology it lags precession maxima by 32° (Figure 2c). Details of phase wheel construct are described in Figure 6.

stants (relative to 65°N summer insolation) in progressively older intervals to account for decreased global ice volume back to 5 Ma. This is appropriate for the obliquity band where both NH and SH summer insolation maxima occur at obliquity maxima; it is irrelevant which hemisphere contains more ice. However, for the oldest interval of time (5 to 2.75 Ma) where SH ice volume dominates, consistent application of the Milankovitch paradigm requires that ice minima lag SH summer insolation maxima for the precession band [*Clemens et al.*, 1996; *Clemens*, 1999]. *Raymo et al.* [2006] successfully model the Plio-Pleistocene global $\delta^{18}O$ record as a function of local summer insolation forcing of both the NH and SH ice sheets, supporting the contention that SH summer insolation forcing of the Antarctic ice sheet is an important factor in generating the Pliocene global benthic $\delta^{18}O$ signal.

[6] We independently infer the time constant for the $\delta^{18}O$ system (5 to 2.75 Ma) from the alkenone-based sea surface temperature (SST) record of *Lawrence et al.* [2006] at Site 846, eastern equatorial Pacific (Figure 2a). During the Pliocene, SST maxima were in phase with $\delta^{18}O$ minima at the obliquity band. By the late Pleistocene, SST maxima lead $\delta^{18}O$ minima by 50°. Two opposing interpretations can be made to account for this long-term 50° phase change at the obliquity band. One could assume that the phase of benthic $\delta^{18}O$ is stationary relative to insolation forcing over the past 5 Ma and assign the long-term 50° drift to equatorial SST. In this case one must explain why the timing of a fast physics variable (SST) changes through time relative to insolation forcing while the timing of a slow physics variable (global ice volume) does not. Alternatively, one could assume that Site 846 SST is phase stationary relative to insolation forcing and attribute the long-term 50° change to benthic $\delta^{18}O$. In this case the $\delta^{18}O$ phase evolution is readily explained as a function of an increasing time constant associated with increased thermal inertia of a

growing NH ice sheet [*Clemens et al.*, 1996; *Imbrie et al.*, 1984; *Lisiecki and Raymo*, 2005]. We choose this latter alternative for three reasons: (1) an increasing time constant through time makes more physical sense for global ice volume than for equatorial SST, (2) the resultant small Pliocene ice sheet time constant is consistent with much reduced global ice mass (as discussed in the next paragraph), and (3) the resultant Pliocene through Pleistocene phase evolution of the Indo-Asian monsoon systems is physically plausible and internally consistent (as discussed in the following sections). We use the observed long-term 50° drift to back-calculate the phase of Pliocene $\delta^{18}O$ relative to insolation forcing as follows.

[7] A decrease of 50° from the SPECMAP late Pleistocene value (−69°) yields an obliquity phase of −19° for $\delta^{18}O$ (−69° + 50° = −19°) which we apply to the older interval (5−2.75 Ma). For the middle interval, we arbitrarily choose a phase value mid way between −69° and −19° (−44°). Phase lags of 19° and 44° indicate ice sheet time constants of 2.3 ka and 6.5 ka at the at the 41 ka frequency band (e.g., 19° = −arc tan $(2\pi)(1/41)(2.3)$) [*Imbrie et al.*, 1984]. In turn, these time constants are used to calculate $\delta^{18}O$ phase lags at the precession band as well (Table 1). For the oldest interval, the 2.3 ka time constant yields a phase lag of 32° at the precession band. In contrast to the currently accepted $\delta^{18}O$ chronology (Figure 2b) [*Lisiecki and Raymo*, 2005], we apply this lag relative to SH summer insolation maxima (Precession maxima; Pmax) (Figure 2c). This phase alignment requires an adjustment of 160° (10.2 ka) to the precession component of the global marine $\delta^{18}O$ chronology prior to 2.75 Ma. First-order confirmation of this approach for deriving the Pliocene phase lag, and its application relative to Pmax, will become clear when it is used to interpret the Pliocene precession band response of the Indian and Asian monsoon systems to insolation forcing; both the WM and SM systems align with the external
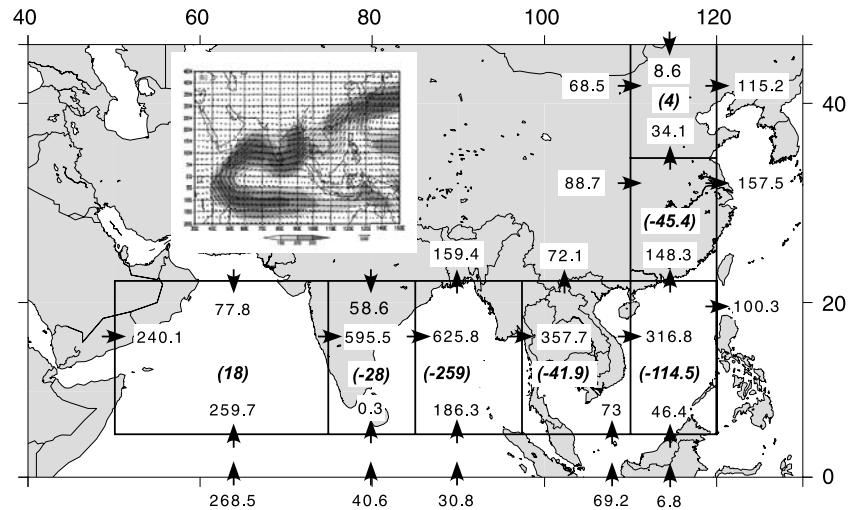
Figure 3. Summer monsoon moisture budget and transport path (inset) after *Ding et al.* [2004]. Moisture budget averaged for 1990 through 1999 (June, July, and August; units are 10^6 kg s^{-1}). The southern Indian Ocean is the dominant moisture (latent heat) source. The Bay of Bengal, Indochina, the South China Sea, and China are all moisture sinks. No significant Pacific moisture source is indicated. Summer monsoon moisture transport patterns (inset) averaged for 1990 through 1999 (the 5th pentad of May through the 2nd pentad of July; units are kg m^{-1} s^{-1}).

forcing, as is expected for an insolation-forced Pliocene system with little NH ice volume [*Kutzbach et al.*, 2007].

4. Monsoon Circulation

[8] The records analyzed here enable us to assess SM and WM variance from both the Indian and east Asian monsoon systems (Figure 1). Dynamically, the SM and WM circulation in both systems is linked by the Indo-Asian low- and high-pressure cells, which they share in common. The strength of the winter high is tied to decreased sensible heating during boreal winter. The strength of the summer low is tied to both the sensible heating of the Indo-Asian continent as well as the release of latent heat into the troposphere during monsoon rains.

[9] Modern regional differences in SM and WM circulation stem from different land-ocean configurations [*Wang et al.*, 2003]. The AS, under the influence of the Indian monsoon, is dominated by north-south winter and summer pressure gradients resulting from the north-south land-ocean configuration. The SCS and CLP, under the influence of the east Asian monsoon, respond to both north-south and east-west land-ocean configurations and associated monsoon pressure gradients. The CLP region is further distinguished by its continental interior location, more directly influenced by continental WM winds.

[10] In spite of these distinctions, recent satellite-based moisture budgets show that SM rainfall in southeast China is coherent and in phase with moisture (latent heat) transport from the Indian Ocean but out of phase with that from the Pacific Ocean [*Liu and Tang*, 2004], a result that is also clearly illustrated in budgets constructed from historical meteorological data [*Ding et al.*, 2004; *Ding and Chan*, 2005; *Emile-Geay et al.*, 2003; *Hu et al.*, 2008]. The SM moisture budget and transport path (Figure 3) clearly

indicate the dominance of the SH Indian Ocean source with cross equatorial flow maxima concentrated in the western equatorial Indian Ocean and moisture sinks in the Bay of Bengal, the South China Sea, and Southeast Asia [*Ding et al.*, 2004]. Thus, the cross equatorial transport of latent heat from the southern Indian Ocean and its release over Indo-Asia [*Bosilovich and Schubert*, 2002; *Liu et al.*, 1994; *Wajsowicz and Schopf*, 2001; *Webster*, 1994] is a major energy source for the entire Indo-Asian SM system [*Hastenrath and Greischar*, 1993]. With regard to paleomonsoons, Clemens and others [*Clemens et al.*, 1991, 1996; *Clemens and Prell*, 2003] have made the case that this southern Indian Ocean energy source is maximized during times of maximum perihelion (+P; 21 December perihelion) as is discussed further in section 6.

[11] Changes in the chemical, physical, biological, and isotopic composition of terrestrial and ocean sediments are driven by changes in large-scale circulation systems such as the Indo-Asian summer and winter monsoons (Figure 1) and are utilized as proxies for past changes in monsoon circulation. The modern northern AS system is dominated by southwest SM winds ($\sim$15 m s^{-1}) which drive strong upwelling-induced surface-ocean productivity along Africa and Arabia [*Honjo et al.*, 1999]. In addition, circulation about the Asian SM low drives strong northwesterly winds over the continent which transport relatively large lithic grains from the surrounding deserts to the Arabian Sea [*Clemens*, 1998]. WM winds are weaker ($\sim$5 m s^{-1}) and more variable in direction. Summer precipitation is minimal over the northern AS except for coastal India where orographic influences predominate. Clockwise surface ocean circulation transports monsoon runoff from the Indus away from the AS core site. Precipitation during the WM is minimal over the entire AS.

[12] The northern SCS system is impacted by both WM and SM dynamics [*Chen and Chen*, 2006; *Qu et al.*, 2007; *Tan and Shi*, 2006; *Tian et al.*, 2005]. Modern WM circulation is characterized by strong northeast winds (8 m s^{-1}) but weak precipitation (2 mm d^{-1}) whereas SM circulation is characterized by weak southerly winds (3 m s^{-1}) and strong precipitation (9 mm d^{-1}). These dynamics yield reduced surface salinities during the modern SM season and increased surface productivity during both the SM (associated with runoff) and the WM (associated with deepening of the mixed layer).

[13] The south central CLP is also impacted by significant SM and WM dynamics [*An et al.*, 2005; *Sun et al.*, 2006]. Annual rainfall is 650 mm with ~70% taking place during the SM. Strong WM outbreaks of cold air associated with frontal systems and the Mongolian cyclonic depression drive intense dust storm activity that transport dust from the northern deserts to the CLP [*Sun et al.*, 2001].

5. Monsoon Proxy Records

[14] The fourteen monsoon proxies included in our synthesis, as well as the benthic $\delta^{18}O$ record, are shown in Figure 4. Analytical methods, age model development, and data archiving are presented in Appendix A. For the CLP, data younger than 3.6 Ma have been previously published [*Sun et al.*, 2006]; data from 5 to 3.6 Ma are new. Briefly, quartz grain size is a well-established proxy for the strength of WM winds [*Sun et al.*, 2006; *Xiao et al.*, 1995]. Similarly, magnetic susceptibility is a well-established SM proxy as reviewed by *An* [2000] although some suggest an influence of carbonate diagenesis prior to 3.6 Ma [*Guo et al.*, 2001]. We find consistent coherence and phase relationships among grain size, magnetic susceptibility, and CaCO$_3$ (not shown) both before and after 3.6 Ma, supporting the utility of the magnetic susceptibility as an orbital-scale SM proxy over the past 5 Ma. Whereas all other records have benthic $\delta^{18}O$ data from the same core, and thus an inherent marine chronology, the CLP records are empirically tied to the marine $\delta^{18}O$ chronology through tuning large quartz grain size (strong WM) directly to ice volume maxima in the benthic $\delta^{18}O$ record [*Sun et al.*, 2006]; this leaves the SM susceptibility record as the independent parameter to be interpreted relative to changes in phase through time. The CLP proxies provide an excellent example of the climatic shift across the 2.75 Ma boundary, clearly illustrating that the SM and WM were nearly in phase prior to 2.75 Ma and nearly 180° out of phase afterward (Figure 5). This 180° change in phase of the SM relative to the WM, also found in some SCS proxies, is independent of absolute chronology and plays a key role in our interpretation of monsoon dynamics as described in following sections.

[15] The AS proxies have been previously published [*Altabet et al.*, 1999; *Clemens et al.*, 1996]. The lithogenic grain size serves as a SM proxy, driven by the strength of the dust-transporting winds associated with cyclonic circulation about the Asian low [*Clemens*, 1998]. The grain size spectra of some samples prior to 1.6 Ma are distinctly bimodal indicating more than one driving mechanism; we exclude these data from our analyses. The *G. bulloides* and biogenic opal records are proxies for the intensity of upwelling-induced productivity driven by unique southwest SM winds blowing along the coast of the Arabian Peninsula. Similarly, $\delta^{15}N$ is a proxy for the intensity of the oxygen minimum zone which is, in turn, linked to upwelling-induced productivity [*Altabet et al.*, 1999, 2002].

[16] While interpretation of the CLP and AS records as either SM or WM proxies is relatively straight forward, interpretation of the SCS proxies is complicated by the influence of both SM and WM circulation on surface productivity and by the fact that Site 1146 is on a continental margin and thus susceptible to the effects of sea level change. The SCS records have not been previously published although the SM and WM proxies presented have been previously interpreted as such by investigators working in the SCS, over various intervals of time. A number of investigators have employed Ba as a paleoproductivity indicator in the SCS [*Calvert et al.*, 1993; *Wehausen and Brumsack*, 2002; *Wei et al.*, 2003] although disagreement exists as to forcing by the SM (nutrient runoff) or the WM (mixed layer deepening). We analyzed both Ba/Al and biogenic Ba accumulation; although they have distinctly different long-term trends, their spectral characteristics yield the same results and are consistent with SM proxies from the Arabian Sea, where the seasonality is clear. Previous investigators have used the $\delta^{18}O$ of seawater [*Tian et al.*, 2006; *Wang et al.*, 1999] and lithogenic accumulation [*Wehausen and Brumsack*, 2002] as indicators sea surface salinity and river runoff in the SCS although both signals are masked by the effects of sea level variation within the late Pleistocene. Biogenic opal has been extensively employed as a SCS productivity indicator although some investigators assign it a SM forcing [*Chen et al.*, 2003a; *Wan et al.*, 2006] whereas others assign it a WM or glacial maximum forcing [*Lin et al.*, 1999; *Tian et al.*, 2005; *Wei et al.*, 2003]. These previous interpretations, based on visual analysis, may not be mutually exclusive. As discussed in following sections, our time series analytical approach indicates that the phase of biogenic opal accumulation is similar to other SM proxies at the precession band, consistent with runoff-induced productivity, but similar to other WM proxies at the obliquity band, consistent with increased productivity driven by deepening of the mixed layer (strengthened WM winds). While not entirely satisfying, there is no a priori reason for expecting similar mechanisms to operate at both orbital bands given their very different impacts on radiation distribution. Finally, we assess chlorin accumulation [*Higginson et al.*, 2003, 2004], total alkenone accumulation [*Hu et al.*, 2002; *Pelejero et al.*, 1999], and Mn accumulation [*Calvert et al.*, 1993] as winter monsoon proxies, consistent with previous interpretations. Here we note that *Calvert et al.* [1993] linked the production of MnO in SCS sediments to overlying productivity and that our results implicate the WM link.

6. Results and Discussion
6.1. Phase Wheel Interpretation

[17] Phase wheels provide a convenient means of summarizing and interpreting coherence and phase relationships
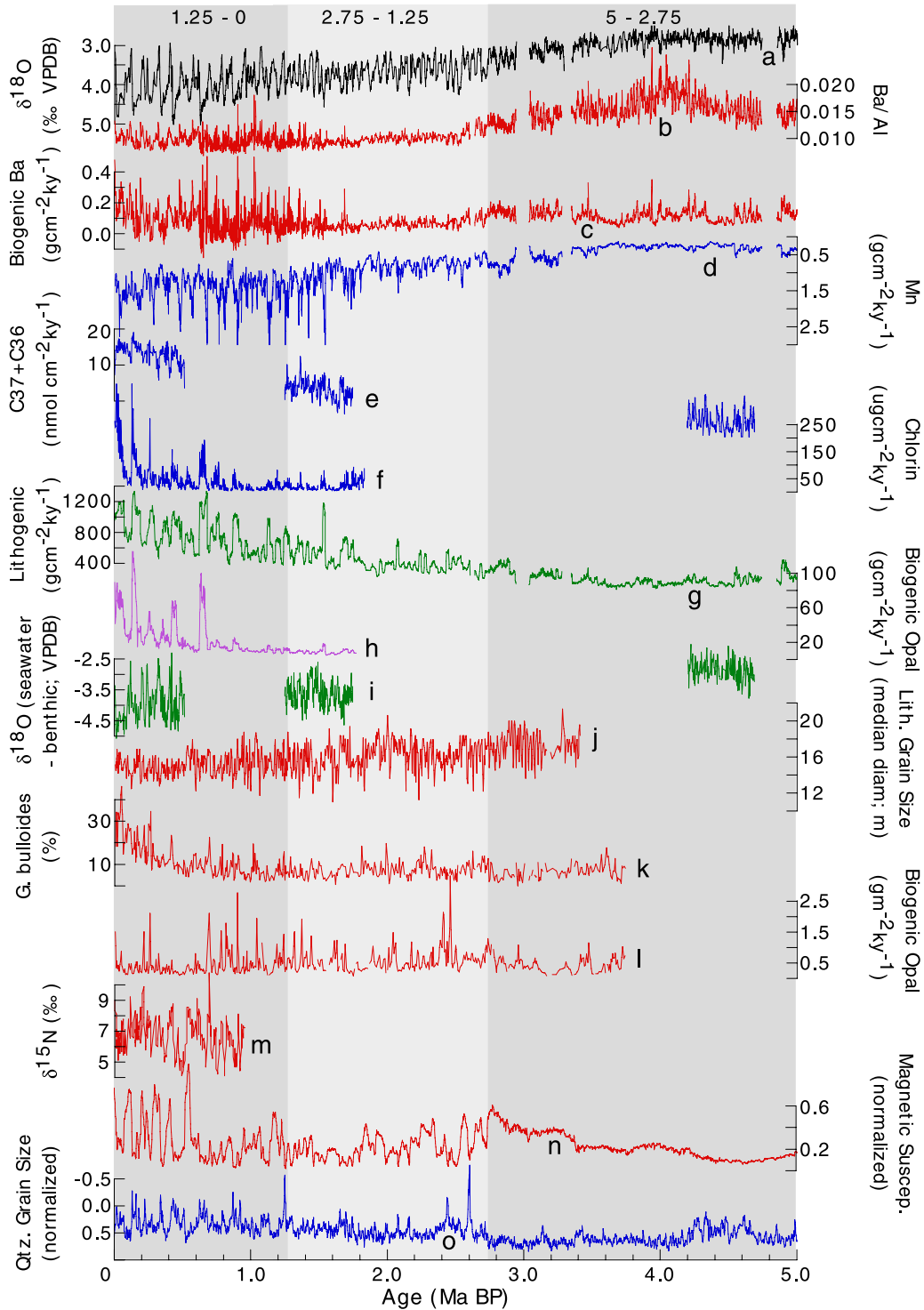
Figure 4. Monsoon and global ice volume ($\delta^{18}O$) proxies. Colors denote proxies that are taken to represent primarily summer monsoon circulation (red), winter monsoon circulation (blue), summer monsoon circulation when not masked by glacial-interglacial sea level effects (green), and summer monsoon circulation at the precession band but winter monsoon circulation at the obliquity band (magenta). Shading denotes the three time intervals over which analyses are conducted. Proxies are plotted such that up represents strong winter dynamics, strong summer dynamics, fresh salinities ($\delta^{18}O_{seawater}$ minus $\delta^{18}O_{benthic}$), and interglacial conditions ($\delta^{18}O$ minima). Proxies are (a–i) from South China Sea Site 1146, (j–m) from Arabian Sea Site 722, and (n and o) from the Chinese Loess Plateau.
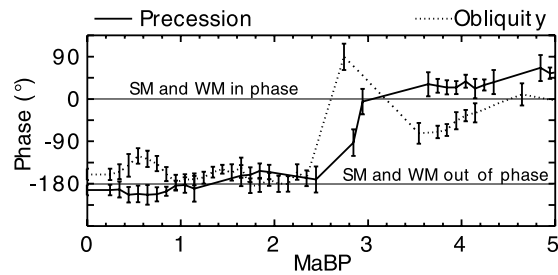
Figure 5. Evolutive cross spectral phase results for summer (magnetic susceptibility) and winter (mean quartz grain size) monsoon proxies from the Chinese Loess Plateau. Phase relationships for the 5 to 2.75 Ma interval indicate that strong summer monsoons and strong winter monsoons occurred at the same time, nearly in phase. After 2.75 Ma, strong summer and winter monsoons were 180° out of phase. These phase relationships are based on data from the same samples and are thus independent of the absolute chronology. Evolutive cross-spectral analyses use a 500 ka window with 100 ka time steps beginning at 250 ka. Phase results and associated errors are plotted at the midpoint of each window provided statistical significance exceeds the 80% CI. Bandwidth is 0.00784 ka^{-1}.

of monsoon proxies relative to one another and relative to potential driving mechanisms (Table 1 and Figure 6). We consider the monsoon response to both fast physics and slow physics variables. Fast physics variables include direct sensible heating and cooling of the Asian landmass [*Webster*, 1987a, 1994, 2006] as well as latent heat export from the southern Indian Ocean as observed in modern Indo-Asian monsoon dynamics [*Bosilovich and Schubert*, 2002; *Ding et al.*, 2004; *Emile-Geay et al.*, 2003; *Liu et al.*, 1994; *Meehl*, 1997; *Simmonds et al.*, 1999; *Wajsowicz and Schopf*, 2001; *Webster*, 1987b, 1994; *Zhu and Newell*, 1998]. All else held constant, fast physics variables operate on a seasonal time scale and should reach maxima at orbital extremes. Alternatively, global ice volume, a slow physics variable, evolves over 10^3 years and involves ice sheet time constants which introduce lags on the order of 10^3 years into the system [*Imbrie et al.*, 1984; *Lisiecki and Raymo*, 2005, 2007]. All else held constant, glacial boundary conditions (the effects of CO_2, ice sheet extent, albedo, and topography) serve to decrease SM strength and increase WM strength [*Dong et al.*, 1996; *Kutzbach and Guetter*, 1986; *Liu et al.*, 2007; *Prell and Kutzbach*, 1992; *Wang et al.*, 2005] although the exact mechanisms are not well known and exceptions do occur; Indian and east Asian summer monsoons, for example, were strengthened during glacial marine isotope stages 6 and 8 [*Clemens and Prell*, 2003; *Masson et al.*, 2000; *Wang et al.*, 2008].

[18] If sensible heating (and cooling) of the Asian landmass were the only factors driving Indo-Asian monsoons, then the strongest summer and winter monsoons would always be in phase with one another and plot at 0° for both orbital bands; the warmest NH summers (InS) and the coldest NH winters (DnW) occur at Pmin and Omax (0° on the phase wheels in Figure 6). If latent heating were the only factor driving Indo-Asian summer monsoons, then the

strongest summer monsoons would occur at −180° on the precession phase wheel and 0° on the obliquity phase wheel as described by *Clemens and Prell* [2003] and denoted by the combination of IsS and DsW in Figure 6. These seasonal relationships (IsS, DsW) yield maximum sensible heating of the southern Indian Ocean during December, January, and February (IsS) followed by minimum sensible heating (cold trade winds) during June, July, August (DsW). This leads to maximum ocean to atmosphere latent heat flux and release of this latent heat during SM precipitation over Asia. Sensitivity tests using a coupled ocean-atmosphere model support this scenario; when SH insolation is increased from December to April, the sea surface temperature (SST) in the southern tropical Indian Ocean remains high from January to July resulting in increase evaporation, increased cross-equatorial moisture transport, and increased SM precipitation [*Liu et al.*, 2006]. If glacial boundary conditions were the only factors driving Indo-Asian monsoon variance, then the strongest summer monsoons would be in phase with ice minima and the strongest winter monsoons would be in phase with ice maxima in Figure 6.

[19] Evaluating the phase evolution of SM and WM proxies over the past 5 Ma allows interpretation of monsoon sensitivity to direct sensible and latent heating as well as the growth of NH ice sheets. We use this framework of forcing and response to document and interpret the evolution of the monsoon over the past 5 million years.

6.2. Interval from 1.25 Ma to Present

[20] Precession band results for the youngest interval (Figure 6a) show that SM proxies cluster near or between ice minima (red arrow) and SH latent heat maxima (IsS,DsW at Pmax). This result indicates that decreased glacial boundary conditions and increased latent heat export from the southern Indian Ocean set the timing of strong summer monsoons within the precession cycle. This does not mean that direct sensible heating of Asia (InS and Pmin) is unimportant; direct sensible heating must initiate monsoonal circulation. The average SM phase over this interval of time is −127° ± 52° (1σ, n = 7). The phases of South China Sea biogenic opal accumulation (BioOpal) and Arabian Sea *G. bulloides* (AS bulloides) contribute much to the large standard deviation, suggesting the possibility of additional variance beyond that contributed by the SM; dissolution may influence the *G. bulloides* phase while winter monsoon variance may influence the BioOpal phase. In any case, the average phase of −127° agrees very well with the average phase of ten SM proxies (−122° ± 16°) previously reported for late Pleistocene records of varying lengths within the past 500 ka from the Arabian Sea (n = 8), South China Sea (n = 1), and the Philippine Sea (n = 1) [*Altabet et al.*, 1995; *Chen et al.*, 2003b; *Clemens et al.*, 1991; *Leuschner and Sirocko*, 2003; *Morley and Heusser*, 1997; *Reichart et al.*, 1998; *Schmiedl and Leuschner*, 2005]. Notably, the only late Pleistocene proxy in disagreement is the Sanbao-Hulu composite speleothem $\delta^{18}O$ record which has a phase of −42° ± 7° when plotted relative to Pmin [*Wang et al.*, 2008]. This suggests the possibility that SM rainfall is not the only influence on cave $\delta^{18}O$ over glacial-interglacial time scales; changes in the ratio of

summer to winter monsoon precipitation as well as changes in precipitation source areas over time may be responsible for the 80° phase difference relative to other late Pleistocene marine records [*Hu et al.*, 2008; *McDermott*, 2004; *Wang et al.*, 2001; S. Clemens et al., Reconciling cave, marine, and loess proxies for summer monsoon strength at the precession band, manuscript in preparation, 2008].

[21] WM proxies on the precession phase wheel (Figure 6a) cluster between ice maxima (blue line) and NH sensible heat minima (DnW at Pmin) indicating that both act to strengthen WM circulation. The antiphase relationship between strong summer and winter monsoons suggests the possibility that the two systems are dynamically linked, strong winter monsoons acting to weaken and/or shorten the following summer monsoon season via the effects of Eurasian snow cover on sensible heat, latent heat (land-atmosphere), and albedo [*Bamzai and Shukla*, 1999; *Barnett et al.*, 1988; *Bush*, 2002].

[22] Obliquity band results for the youngest interval (Figure 6d) show that SM proxies cluster between ice

minima (red arrow) and sensible/latent heat maxima (InS and IsS,DsW at Omax) indicating that all three act in concert to strengthen SM circulation. All WM proxies cluster between ice maxima (blue line) and sensible heat minima (DnW at Omax) indicating that both act to strengthen WM circulation.

[23] SCS surface salinity (Fresh SSS) and lithogenic accumulation (Lith.) have high coherence and near zero-phase relationships with ice maxima at both orbital bands (Figures 6a and 6d) implicating sea level forcing. In this case, sea level lowstands yield increased shelf to slope lithogenic transport as well as fresher sea surface salinity due to restricted outflow of fresh surface waters through Indonesia [*Wang*, 1999]. These two variables are progressively less influenced by ice volume/sea level forcing in the earlier intervals, prior to the initiation of large amplitude NH glacial-interglacial cycles. Finally, SCS biogenic opal (Bio-Opal) has a phase more consistent with other WM indicators at the obliquity band (Figure 6d) but with SM indicators at the precession band (Figure 6a). This distinction is more
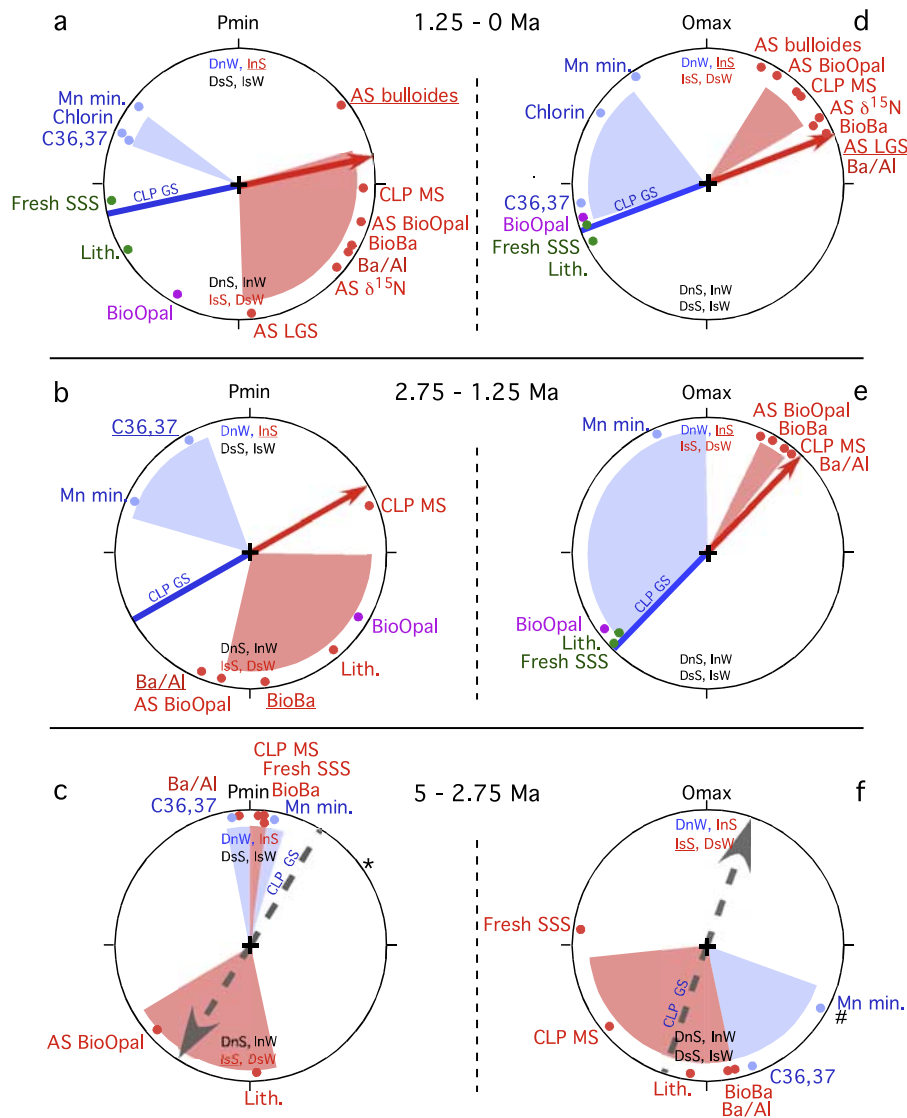
Figure 6

evident in the middle interval and entirely consistent with previous publications having interpreted biogenic opal as both SM and WM indicators.

6.3. Interval from 2.75 to 1.25 Ma

[24] Some proxies are not significantly coherent within this middle interval, likely because of rapidly growing ice volume and rapidly evolving phase relationships. Nevertheless, the overall phase responses are very similar to those of the youngest interval. Precession band results (Figure 6b) show that SM proxies cluster near or between ice minima and SH latent heat maxima (IsS, DsW at Pmax). All WM proxies cluster between ice maxima and NH sensible heat minima (DnW at Pmin). Obliquity band results (Figure 6e) show that SM proxies cluster between ice minima and sensible/latent heat maxima (InS and IsS,DsW at Omax). WM proxies plot between ice maxima and sensible heat minima (DnW at Omax).

[25] SCS lithogenic accumulation at the precession band (Figure 6b) is shifted 105° relative to the youngest interval, plotting with other SM proxies. This implies that the amplitude of sea level change at the precession band is not large enough to drive significant shelf to slope transport; instead, lithogenic flux is driven by summer monsoon runoff. At the obliquity band, SCS lithogenic accumulation and Fresh SSS remain tied to ice maxima indicating that the amplitude of sea level change at the obliquity band serves to restrict outflow and increase shelf to slope lithogenic transport during lowstands. This is not the case in the earliest interval where fresh SSS plots closer to other SM proxies.

6.4. Interval from 5 to 2.75 Ma

[26] Precession band results for the early interval (Figure 6c) show that WM and SM proxies from the CLP and SCS are in phase with one another and with direct sensible heat forcing (InS at Pmin). In addition, the only coherent AS SM proxy and one of the SCS SM proxies plot near the SH latent heat maxima (IsS, DsW at Pmax). Three primary conclusions are drawn from these relationships. First, the in-phase SM WM relationship must be driven by direct NH insolation forcing for which increased NH summer insolation (InS) and decreased NH winter insolation (DnW) both occur at Pmin. Most of the SM proxies no longer plot anywhere near ice minima as in the two younger intervals; the small amount of extant NH ice volume likely plays no significant role in determining the timing of monsoon maxima. Second, this in-phase relationship between summer and winter monsoons and direct sensible forcing is achieved only if the Pliocene marine $\delta^{18}O$ chronology is revised to be consistent with the Milankovitch paradigm linking the phase of ice growth and decay in the precession band to summer insolation in the Southern Hemisphere (IsS), where the dominant Pliocene ice mass resides. The

Figure 6. (a−f) Cross-spectral coherence and phase wheel summaries showing the SM and WM response to insolation forcing and global ice volume evolution at the Earth orbital obliquity (41 ka) and precession (23 ka) periods for the intervals 5 to 2.75 Ma, 2.75 to 1.25 Ma, and 1.25 Ma to present. The precession index is defined as $\Delta e\sin\omega$ where ω is the longitude of perihelion measured from the moving vernal point and e is the eccentricity of Earth's orbit about the Sun [*Berger*, 1977; *Laskar et al.*, 1993]. Obliquity is the tilt of Earth's axis with respect to the plane of the ecliptic. Zero phase is set at precession minima (Pmin; $\omega = 90°$, 21 June perihelion) and obliquity maxima (Omax). By definition, Pmax and Omin are 180° from these locations. Negative phases are measured in the clockwise direction representing temporal lags. For example, in Figure 6a, minimum ice volume ($\delta^{18}O$; red arrow) has a phase of −78° relative to Pmin indicating a 5 ka lag (−78°/360° × 23 ka). The timing of seasonal hemispheric insolation extremes are denoted by abbreviated text at orbital maxima and minima (D, decreased; I, increased; n, Northern Hemisphere; s, Southern Hemisphere; W, winter; S, summer). Abbreviated text in red indicate maxima in SM forcing while abbreviated text in blue indicate maxima in winter monsoon forcing. For example, precession minima (0° in Figures 6a−6c) are characterized by DnW (decreased Northern Hemisphere winter insolation) and InS (increased Northern Hemisphere summer insolation) while precession maxima (180° in Figures 6a−6c) are characterized by IsS (increased Southern Hemisphere summer insolation) and DsW (decreased Southern Hemisphere winter insolation). At the obliquity band, InS applies only to areas north of 14°N while IsS applies only to areas south of 14°S. Red arrows represent the phase of benthic $\delta^{18}O$ minima (ice volume minima) while blue lines represent the phase of benthic $\delta^{18}O$ maxima (ice volume maxima). The underlined abbreviations (*InS* and *IsS*) signify the sensible heat forcing to which ice volume responds, InS when Northern Hemisphere ice volume is dominant and IsS when Southern Hemisphere ice volume is dominant. The ice volume indicators are dashed and gray in the 5 to 2.75 Ma interval signifying that NH ice volume, and its potential impact on Indo-Asian monsoon circulation, is minimal during this interval. Dots, and associated labels, indicate the phase of monsoon proxy maxima measured relative to $\delta^{18}O$ minima, provided cross-spectral coherence exceeds the 80% confidence interval. The prefix AS denotes Arabian Sea, the prefix CLP denotes Chinese Loess Plateau. All other proxies are from the South China Sea. Underlined proxies are not coherent with $\delta^{18}O$ but are coherent with orbital parameters; in this case, the phase is still plotted relative to $\delta^{18}O$ by taking into account the phase of $\delta^{18}O$ relative to the orbital parameter. Red dots and labels indicate dominant summer monsoon forcing, blue dots and labels indicate dominant winter monsoon forcing, green dots and labels indicate dominant sea level forcing, and magenta dots and labels indicate mixed forcing with a dominant winter monsoon forcing at the obliquity band and a dominant summer monsoon forcing at the precession band. Shaded wedges indicate the 1σ (standard deviation) of summer monsoon and winter monsoon proxy phase estimates within each interval of time. The asterisk in Figure 6c represents the phase of ice minima following the chronostratigraphy of *Lisiecki and Raymo* [2005]; this is the only interval where our ice volume phase estimate differs significantly from theirs. The number symbol in Figure 6f represents the phase of observed South China Sea SST maxima (Site 1146).
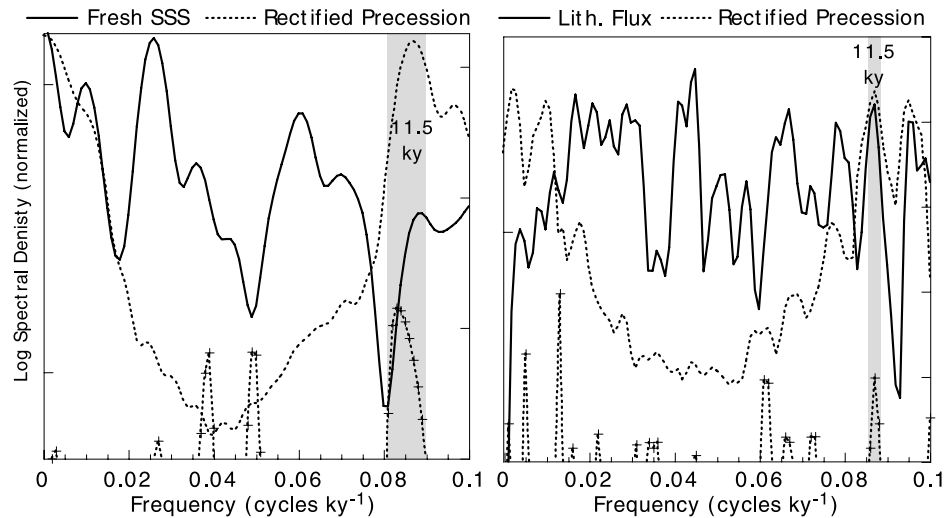
Figure 7. Cross-spectral analysis of South China Sea lithogenic flux (5 to 2.75 Ma) and sea surface salinity (4.7 to 4.2 Ma) relative to rectified orbital precession. The precession index, when rectified about the mean, yields a robust semiprecession target for comparison purposes. Both the lithogenic flux and sea surface salinity records are coherent above the 95 CI at the semiprecession (11.5 ka^{-1}) period indicating two strong summer monsoons within each precession cycle. Prior to analysis, the lithogenic record was detrended with a first difference filter to remove low-frequency variance.

asterisk in Figure 6c represents the phase of ice minima in the most recent revision of the global $\delta^{18}O$ time scale [*Lisiecki and Raymo*, 2005]. To visualize the implications of such a phase, rotate the ice minima arrow and all other proxies by $\sim160°$ counterclockwise such that the arrow and asterisk match. In this case, the WM proxies would no longer be in phase with decreased NH winter insolation (DnW) and the SM proxies no longer in phase with increased NH summer insolation (InS); SM and WM maxima would be 160° out of phase with direct insolation forcing, with no plausible explanation. The tight phase coupling between the monsoon indicators and Pmin supports our use of Site 846 obliquity band SST and $\delta^{18}O$ phase relationships (section 3) to infer the ice volume time constant and hence the phase of $\delta^{18}O$ at both orbital bands, including our assumption of phase stationary Site 846 SST and an increasing $\delta^{18}O$ time constant as ice volume grows into the Pleistocene. Third, the result indicating strong SM circulation at both Pmin and Pmax indicates that the SM is strong twice within each precession cycle, at the timing of maximum NH sensible heating (InS at Pmin) and max SH latent heat export (IsS, DsW at Pmax). This conclusion is consistent with the spectra of both the SCS salinity and lithogenic flux records, both of which have significant 11.5 ka spectral variance (Figure 7).

[27] Obliquity band results for the early interval (Figure 6f) show that SM and WM phases are distributed about Omin. Relative to the middle interval, SCS lithogenic accumulation and fresh SSS are no longer in phase with one another and with ice maxima; rather, they now have phases similar to other SCS SM proxies and are interpreted as such. AS proxies are not coherent within this interval.

[28] Obliquity minima are characterized by decreased NH summer insolation (DnS) and increased NH winter insolation (InW). In contrast with the precession results, these phase results appear in conflict with direct sensible (InS) and latent heat (IsS, DsW) forcing which occur at Omax. Insight into this apparent contradiction is gained from the results of a 284 ka time-dependent model experiment using the global fully coupled ocean-atmosphere (FOAM) model in which only insolation changes over time (Figure 8) [*Kutzbach et al.*, 2007]. We take this experiment as a first-order simulation of Pliocene circulation in that NH ice volume is minimal and CO_2 is unchanged. Figure 8b shows the phase of obliquity forcing in the same context as the phase wheels, such that obliquity-driven insolation maxima north of 14°N occurs at Omax (InS) whereas obliquity-driven insolation maxima south of 14°N occurs at Omin (IsW). From an insolation standpoint, all the monsoon proxy sites are at or north of this boundary, hence the apparent conflict with the observed phases in Figure 6f. However, when insolation is translated into model surface temperature, this boundary shifts significantly north such that all sites lie near or south of the boundary where the model results show maximum summer warmth at Omin (Figure 8e) and maximum summer precipitation over the majority of southeast Asia and the SCS at Omin (Figure 8h). These results are consistent with the observed SM phases and the phase of SCS Site 1146 SST (Figure 6f). Finally, model winter monsoon results show enhanced east Asian and northern SCS precipitation at Omin (Figure 8i) suggesting the possibility that the WM productivity proxies are responding to runoff during this Pliocene interval. These response patterns of the temperature and precipitation relative to orbital forcing are associated with regional dynamics of the atmosphere as detailed by G.-S. Chen et al. (Modeling the evolutionary response of Asian monsoon to obliquity forcing in a coupled GCM, manuscript in preparation, 2008). The complex pattern of the simulated climate response, especially in precipitation, suggests the
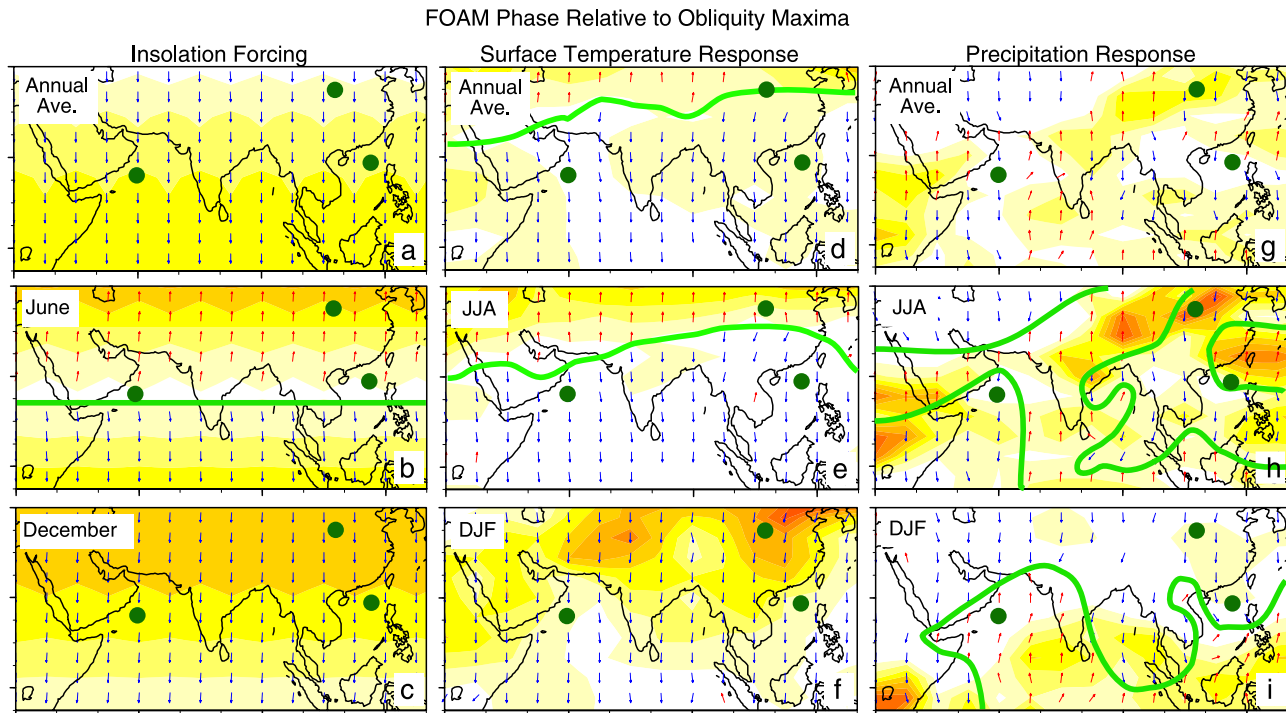
Figure 8. Obliquity band phase results for monthly average (a–c) insolation, (d–f) surface temperature, and (g–i) precipitation from a 280 ka time-dependent experiment using FOAM, a fully coupled global ocean-atmosphere general circulation model. Each vector represents the cross-spectral phase result of a parameter relative to obliquity maximum (0°). Here the color scheme does not relate to summer or winter monsoons in any way; colors simply delineate vectors that generally point more toward 0° (red) or more toward 180° (blue). Yellow shading indicates parameter variance standardized by obliquity variance. The insolation phase vectors are consistent with the hemispheric insolation extremes denoted on Figure 6 phase wheel summaries. For example, the upward directed (0°) red vectors north of 14°N in Figure 8b denote the phase of maximum June insolation and correlate directly with InS at 0° on the obliquity phase wheels (Figures 6d–6f). Similarly, the downward directed (180°) blue vectors in Figure 8c denote the phase of maximum December insolation which correlates directly to InW at 180° on the obliquity phase wheels (Figures 6d–6f).

need for caution in extrapolating a regional climate record to large-scale climate response in the past.

7. Conclusions

[29] 1. The timing of strong Indian and east Asian monsoons (summer and winter) is nonstationary relative to orbital insolation forcing over the past 5 Ma. The timing (phase) of strong Indian and east Asian monsoons evolved similarly in response to the shift from SH ice volume dominance during the Pliocene to NH ice volume dominance during the Pleistocene indicating a strong coupling at orbital time scales.

[30] 2. Prior to ~2.75 Ma, when the dominant ice mass resided in the Southern Hemisphere, the Indian and east Asian summer and winter monsoons were in phase with one another and strongest at orbital extremes, reflecting the influence of fast physics variables (latent and sensible heating). The summer monsoon was characterized by a semiprecession signal, strengthened both at precession minima, in response to sensible heating of Asia, and at precession maxima, in response to latent heat export from

the southern Indian Ocean. The winter monsoon strengthened at precession minima, in direct response to sensible cooling of Asia. At the obliquity band, the summer monsoon strengthened at obliquity minima, in response to warming of the tropics at times of reduced axial tilt, an inference based on time-dependent climate model results. Similarly, the winter monsoon strengthened at obliquity minima, characterized by increased winter precipitation, also an inference based on climate model results.

[31] 3. After ~2.75 Ma, as Northern Hemisphere ice volume expanded, the timing of strong winter and summer monsoons drifted apart from one another and away from orbital extremes; the phase of strong winter monsoons shifted toward ice maxima and the phase of strong summer monsoons shifted toward ice minima, reflecting the combined influence of fast physics variables (latent and sensible heating) and slow physics variables (glacial boundary conditions). At the precession band, Indo-Asian summer monsoon maxima occurred mid way between ice minima (minimum glacial boundary conditions) and precession maxima (southern Indian Ocean latent heating) while the phase of winter monsoon maxima occurred mid way

between ice maxima (maximum glacial boundary conditions) and precession minima (sensible cooling over Asia). At the obliquity band, summer monsoon maxima occurred between ice minima (minimum glacial boundary conditions) and obliquity maxima (the combined effects of Indian Ocean latent heat export and Asian sensible heating) while winter monsoon maxima occurred mid way between ice maxima (maximum glacial boundary conditions) and obliquity maxima (Asian sensible cooling).

[32] 4. The change from in-phase Pliocene summer and winter monsoons to out-of-phase Pleistocene summer and winter monsoons is internal to the various data sets; the phase change is independent of the global marine $\delta^{18}O$ chronology. However, understanding the phase shift in the context of orbital forcing and global ice volume evolution depends very much on the global marine $\delta^{18}O$ chronology. Consistent application of the Milankovitch paradigm and phase analysis of equatorial Pacific SST (relative to benthic marine $\delta^{18}O$) suggest the need to revise the precession component of the global marine $\delta^{18}O$ chronology by $160°$ (10.2 ka) prior to 2.75 Ma. Only when these revisions are incorporated is the in-phase relationship between Pliocene summer and winter monsoon strength consistent with a direct, fast physics response to orbital forcing at the precession band, an intuitive result that is supported by modeling. We take this as strong support for our suggested revision of the global marine chronology.

Appendix A

A1. Methods

A1.1. Sampling

[33] To achieve a target sample resolution of $\sim$2 ka, the Site 1146 splice was sampled every 50 cm from the top to 1146B, 6H, 6, 103.5 cm (57.235 mcd), every 20 cm from there to 1146C, 9H, 4, 138.5 cm (86.935 mcd), every 15 cm from there to 1146B, 12H, 5, 48.5 cm (115.785 mcd), every 10 cm from there to 1146C, 23X, 5, 73.5 cm (228.525 mcd), and every 5 cm from there to 1146C, 29X, 7, 13 cm (314.34 mcd). Excluding recognized core breaks, this yields an average sample resolution of 1.9 ± 1.4 ka.

A1.2. Planktonic Stable Isotopes

[34] Isotope samples were picked from 10 cm^3 samples that were freeze dried, disaggregated, washed in tap water, sieved at 150 μm, dried, and stored in glass vials. Two separate size fractions of *Globigerinoides ruber* (white) were selected (212 to 355 μm and >355 μm) in order to have sufficient material for isotopic analysis with replicates where necessary. Analyses shallower than 1146C 19X 4, 63.5 cm (185.075 mcd) are predominantly from the >355 μm fraction whereas analyses deeper are predominantly from the 212 to 355 μm fraction. Isotopic analyses were completed on two to twelve individuals (typically seven) in the 212 to 355 μm size range and two to seven individuals (typically four) in the >355 μm size range, depending on availability. Deeper than 1146C 28X 5, 3 cm (298.31 mcd) analyses were done on *Globigerinoides sacculifer* in the 212 to 355 size fraction using 3 to 5 individuals (typically 4). For each sample, foraminifers were placed into the

bottom of a reaction vial and broken using a glass pestle. Thirty μL of 5% H_2O_2 was added and allowed to react for 30 min at which time 60 μL of ethanol was added, the sample sonified for 30 s, and all liquid drawn off using a micropipette. The sample was then dried at 50°C.

[35] A total of 3584 analyses (including duplicate and triplicate analyses) were conducted on 3034 samples. A total of 70 *G. ruber* samples were measured for both the 212 to 355 μm and >355 μm size fractions. On the basis of the median differences within these 70 paired analyses, we convert data in the >355 μm size fraction to values consistent with the 212 to 355 μm size fraction by subtracting 0.61 from the $\delta^{13}C$ values and adding 0.23 to the $\delta^{18}O$ values. A total of 25 paired *G. ruber* and *G. sacculifer* analyses were undertaken in the interval between 1146C 28X, 4, 48 cm (297.27 mcd) and 1146C 29X 1, 133 cm (306.54 mcd). On the basis of the median differences within these 25 paired analyses, we convert the *G. sacculifer* data to values consistent with the *G. ruber* data by subtracting 0.35 from the $\delta^{13}C$ values and subtracting 0.27 from the $\delta^{18}O$ values. All values are plotted and reported relative to *G. ruber* (212 to 355 μm size fraction).

A1.3. Benthic Stable Isotopes

[36] Two species of benthic foraminifers were picked in the >150 μm size fraction (*Cibicides wuellerstorfi* and *Uvigerina peregrina*) in order to have sufficient material for isotopic analysis with replicates where necessary. Isotopic analyses were completed on one to five individuals depending on availability. For each sample, foraminifers were placed into the bottom of a reaction vial and broken using a glass pestle. Thirty μL 5% H_2O_2 was added and allowed to react for 30 min at which time 60 μL ethanol was added, the sample sonified for 30 s, and all liquid drawn off using a micropipette. The sample was then dried at 50°C. A total of 3382 analyses (including duplicate and triplicate analyses) were conducted on 2535 samples. Of the 3382 analyses, 1406 were on *C. wuellerstorfi* and 1976 on *U. peregrina*. Analysis of 533 *C. wuellerstorfi* and *U. peregrina* pairs indicates linear, long-term trends in the isotopic offsets between these species at ODP Site 1146. At the core top, 0.99 is subtracted from *C. wuellerstorfi* $\delta^{13}C$ to make it consistent with U. peregrina. At the bottom of the studied section ($\sim$314 mcd, 5 Ma.), 0.45 is subtracted from *C. wuellerstorfi* $\delta^{13}C$ to make it consistent with U. peregrina. At the core top, 0.63 is added to *C. wuellerstorfi* $\delta^{18}O$ to make it consistent with *U. peregrina*. At the bottom of the studied section ($\sim$314 mcd, 5 Ma.), 0.53 is added to *C. wuellerstorfi* $\delta^{18}O$ to make it consistent with *U. peregrina*. Between the core top and the bottom of the studied section, these carbon and oxygen values were adjusted linearly according to depth. In practice, the long-term trend in the $\delta^{18}O$ offset is small and makes little difference whereas that for $\delta^{13}C$ is significant. All data are plotted and reported relative to *U. peregrina*.

A1.4. Isotopic Analysis

[37] Samples were run in batches of approximately 40 on a Finnigan MAT 252 equipped with a Carbonate (Kiel) III autosampler that reacts samples in individual reaction

vessels at 70°C using H_3PO_4. External reproducibility based on repeated analysis of NBS-19 yielded $\delta^{13}C$ values of 1.94 ± 0.02 and $\delta^{18}O$ values of -2.23 ± 0.04 (1σ, n = 13). External reproducibility based on repeated analysis of Brown Yule Marble (BYM, 63–150 μ) yielded $\delta^{13}C$ values of -2.28 ± 0.03 and $\delta^{18}O$ values of -6.56 ± 0.06 (1σ, n = 230). External reproducibility based on repeated analysis of Carrara Marble (63–150 μ) yielded $\delta^{13}C$ values of 2.03 ± 0.02 and $\delta^{18}O$ values of -1.93 ± 0.05 (1σ, n = 225). External reproducibility based on replicate analysis of planktonic foraminifer samples is ±0.15 for both $\delta^{13}C$ and $\delta^{18}O$ (average half-range, n = 158). External reproducibility based on replicate analysis of benthic foraminifer samples is ±0.07 and ±0.05 for $\delta^{13}C$ and $\delta^{18}O$ respectively (average half-range, n = 71). The Carrara and BYM in-house standards have been calibrated to National Institute of Standards and Technology (NIST) isotopic reference material NBS-19 for conversion to the (Vienna) Peedee belemnite (VPDB) scale. All data plotted and reported are in per mille (‰) notation relative to VPDB.

A1.5. Chemical and Isotopic Proxies

[38] Major and minor elemental analyses were run on a JY2000 Ultrace Inductively Coupled Plasma Atomic Emission Spectrometer equipped with an autosampler at Brown University. Our procedures generally follow those detailed by *Murray et al.* [2000]. Approximately 0.04 g of previously freeze-dried, ground, and homogenized sample was fused at 1070°C in a graphite crucible in the presence of approximately 0.16 g of lithium metaborate flux. The resulting molten bead was immediately digested in 10% nitric acid on a shaker table, filtered at 0.45 microns, and diluted to approximately 4000X. Lithium metaborate blanks were processed with every batch of samples. One in-house sediment sample (from marine core RC2709CC) and a set of eight standard reference material sediments were processed with every other batch of samples. Sediment standards include 1646a (estuarine sediment), 2711 (Montana soil), BCSS-1 (marine sediment), MAG-1 (marine sediment), NIST-1c (argillaceous limestone), SCO-1 (Cody shale), SDO-1 (Devonian Ohio shale), and SGR-1 (Green River shale). The standards were used both for daily run calibration of the JY2000 and for monitoring drift over the course of each run. Data from each run were reduced offline by construction of calibration curves for each element and including both blank and drift corrections. Analyses were conducted using the following emission lines (nm): Al (396.152), Ba (455.403), Ca (317.933), Fe (259.94), K (766.49), Mg (285.213), Mn (257.61), Na (589.592), Si (251.611), Sr (407.771), Ti (308.803). Replicate analysis from raw sample yields the following external reproducibility (n = 83; as % of absolute value): Al ($\pm1.2\%$), Ba ($\pm2.8\%$), Ca ($\pm3.2\%$), Fe ($\pm1.7\%$), K ($\pm1.6\%$), Mg ($\pm1.5\%$), Mn ($\pm1.5\%$), Na ($\pm1.7\%$), Si ($\pm1.6\%$), Sr ($\pm1.8\%$), Ti ($\pm1.4\%$). The lithogenic percent was determined both by difference (100 – $CaCO_3$ – biogenic opal – salt) and by Al content using post-Archean crustal compositions from *Taylor and McClennan* [1985]. Both methods produced extremely similar results. $CaCO_3$ was derived by regressing Ca against coulometer-measured

$CaCO_3$ (%$CaCO_3$ = 2.457*Ca + 3.858; n = 539, R^2 = 0.96). Biogenic Ba is calculated as that in excess of the amount in post-Archean crustal composition [*Taylor and McClennan*, 1985] where percent biogenic Ba = Ba – Al*.006498. Spectrally, this yields the same results as Ba/Al. Salt content is similarly calculated where %NaCl = 2.542*Na – 0.089*Al.

[39] Biogenic opal was measured at Brown University by spectrophotometer using procedures detailed by *Murray et al.* [1995]. External reproducibility is $\pm3.5\%$ of the opal concentration value (based on raw sample replicates, n = 6).

[40] Chlorin analyses were made at the University of Massachusetts, Dartmouth, School for Marine Science and Technology following sediment extraction and HPLC methodologies detailed by *Higginson et al.* [2003]. This methodology yields a standard deviation of less than 3% for analyses of separate aliquots from the same sample interval.

[41] Alkenone concentration and sea surface temperature (SST) analyses were conducted at Brown University following procedures detailed by *Herbert and Schuffert* [1998] and *Lawrence et al.* [2006]. Reproducibility derived from multiple extractions of a marine sediment standard (n = 50) yields ±0.2°C for SST and ±0.2 n molg^{-1} for C37total, consistent with that reported by *Herbert and Schuffert* [1998].

[42] SST, benthic $\delta^{18}O$, and planktonic $\delta^{18}O$ were used to estimate sea surface salinity (SSS; actually $\delta^{18}O_{surfacewater}$ minus $\delta^{18}O_{benthic}$) using an empirical $\delta^{18}O_{seawater}$ equation from *Bemis et al.* [1998], confirmed by the sediment trap work of *Thunell et al.* [1999] as reported and used by both *Lea et al.* [2002] and *Tian et al.* [2006] where $\delta^{18}O_{seawater}$ minus $\delta^{18}O_{benthic}$ (VPDB) = ((SST – 16.5 + 4.8*$\delta^{18}O_{planktonic}$)/4.8) – $\delta^{18}O_{benthic}$. Subtracting the $\delta^{18}O_{benthic}$ record serves to remove the global (glacial interglacial) $\delta^{18}O_{seawater}$ signal but introduces the long-term global deep water temperature signal preventing interpretation of the long-term trend in terms of salinity change. We interpret only the phase results of this record in terms of the timing of changes in the salinity of surface waters.

[43] All mass accumulation rates (gcm^{-2}ky^{-1}) are calculated as the dry bulk density (DBD; g cm^{-3}) multiplied by the linear sedimentation rate (cm ka^{-1}) and the variable concentration where DBD for a given sample depth is derived from a 15% weighted smooth through shipboard data plotted as a function of depth.

A2. Age Model

[44] The Site 1146 age model is based on tuning the 41-ka component of $\delta^{18}O$ to orbital obliquity incorporating the SPECMAP-defined lag of $-69°$ [*Imbrie et al.*, 1984] for $\delta^{18}O$ minima (ice minima) relative to obliquity maxima. The obliquity tuning target is from the *Laskar et al.* [1993] orbital solution (La93 0,1). Age control points are located midway between obliquity maxima and obliquity minima; this translates to 245 age control points over the past 4.985 Ma, or one every 20.3 ka on average. Tuning was accomplished by iteratively adjusting the depths of the benthic $\delta^{18}O$ record associated with these set age control points in order to maximize coherence and phase at the obliquity band. Simultaneously, the precession band $\delta^{18}O$

amplitude in both the benthic and planktonic records was monitored to prevent overtuning at the obliquity band such that amplitude at the precession band was diminished. Unlike *Lisiecki and Raymo* [2005], this tuning approach does not attempt to account for the change in ice sheet time constant over time and does not constrain the phase at the precession band. Rather, these variables are open for interpretation in the context of this work.

A3. Data Archive

[45] Data are archived at http://www.ncdc.noaa.gov/paleo/paleo.html.

References

Altabet, M. A., et al. (1995), Climate-related variations in denitrification in the Arabian Sea from sediment $^{15}N/^{14}N$ ratios, *Nature*, *373*, 506–509, doi:10.1038/373506a0.

Altabet, M., et al. (1999), Climatically linked oscillations in Arabian Sea denitrification over the last 1 m.y: Implications for marine N Cycle, *Paleoceanography*, *14*, 732–743, doi:10.1029/1999PA900035.

Altabet, M. A., et al. (2002), The effect of millennial-scale changes in Arabian Sea denitrification on atmospheric CO_2, *Nature*, *415*, 159–162, doi:10.1038/415159.

An, Z. S. (2000), The history and variability of the east Asian paleomonsoon climate, *Quat. Sci. Rev.*, *19*, 171–187, doi:10.1016/S0277-3791(99)00060-8.

An, Z., et al. (2005), Multiple expansions of C4 plant biomass in east Asia since 7 Ma coupled with strengthened monsoon circulation, *Geology*, *33*(9), 705–708, doi:10.1130/G21423.1.

Bamzai, A. S., and J. Shukla (1999), Relation between Eurasian snow cover, snow depth, and the Indian summer monsoon: An observational study, *J. Clim.*, *12*, 3117–3132, doi:10.1175/1520-0442(1999)012<3117:RBESCS>2.0.CO;2.

Barnett, T. P., et al. (1988), The effect of Eurasian snow cover on global climate, *Science*, *239*, 504–508, doi:10.1126/science.239.4839.504.

Bemis, B. E., et al. (1998), Reevaluation of the oxygen isotopic composition of planktonic foraminifera: Experimental results and revised paleotemperature equations, *Paleoceanography*, *13*, 150–161.

Berger, A. (1977), Long-term variations of the earth's orbital elements, *Celestial Mech.*, *15*, 53–74, doi:10.1007/BF01229048.

Bosilovich, M. G., and S. D. Schubert (2002), Water vapor tracers as diagnostics of the regional hydrological cycle, *J. Hydrometeorol.*, *3*, 149–165, doi:10.1175/1525-7541(2002)003<0149:WVTADO>2.0.CO;2.

Bush, A. B. G. (2002), A comparison of simulated monsoon circulations and snow accumulation in Asia during the mid-Holocene and at the Last Glacial Maximum, *Global Planet. Change*, *32*(4), 331–347, doi:10.1016/S0921-8181(02)00074-7.

Calvert, S. E., et al. (1993), Geochemistry of the surface sediments of the Sulu and South China seas, *Mar. Geol.*, *114*(3–4), 207–211, doi:10.1016/0025-3227(93)90029-U.

Chen, M., et al. (2003a), Development of east Asian summer monsoon environments in the late Miocene: Radiolarian evidence from Site 1143 of ODP Leg 184, *Mar. Geol.*, *201*(1–3),

169–177, doi:10.1016/S0025-3227(03)00215-9.

Chen, M.-T., et al. (2003b), 500,000-year records of carbonate, organic carbon, and foraminiferal sea-surface temperature from the southeastern South China Sea (near Palawan Island), *Palaeogeogr. Palaeoclimatol. Palaeoecol.*, *197*(1–2), 113–131, doi:10.1016/S0031-0182(03)00389-4.

Chen, Y.-L., and H.-Y. Chen (2006), Seasonal dynamics of primary and new production in the northern South China Sea: The significance of river discharge and nutrient advection, *Deep Sea Res., Part I*, *53*, 971–986, doi:10.1016/j.dsr.2006.02.005.

Clemens, S. C. (1998), Dust response to seasonal atmospheric forcing: Proxy evaluation and calibration, *Paleoceanography*, *13*, 471–490, doi:10.1029/98PA02131.

Clemens, S. C. (1999), An astronomical tuning strategy for Plio-Pleistocene sections: Implications for global-scale correlation and phase relationships, *Philos. Trans. R. Soc. London, Ser. A*, *357*, 1949–1974, doi:10.1098/rsta.1999.0409.

Clemens, S. C., and W. L. Prell (2003), A 350,000 year summer-monsoon multi-proxy stack from the Owen Ridge, northern Arabian Sea, *Mar. Geol.*, *201*(1–3), 35–51, doi:10.1016/S0025-3227(03)00207-X.

Clemens, S. C., et al. (1991), Forcing mechanisms of the Indian Ocean monsoon, *Nature*, *353*, 720–725, doi:10.1038/353720a0.

Clemens, S. C., et al. (1996), Nonstationary phase of the Plio-Pleistocene Asian monsoon, *Science*, *274*, 943–948, doi:10.1126/science.274.5289.943.

Ding, Y., and J. C. L. Chan (2005), The east Asian summer monsoon: An overview, *Meteorol. Atmos. Phys.*, *89*, 117–142, doi:10.1007/s00703-005-0125-z.

Ding, Y., et al. (2004), Overview of the South China Sea Monsoon Experiment, *Adv. Atmos. Sci.*, *21*, 343–360, doi:10.1007/BF02915563.

Dong, B., et al. (1996), The changes of monsoonal climates due to Earth's orbital perturbations and ice age boundary conditions, *Paleoclimates*, *1*, 203–240.

Emile-Geay, J., M. A. Cane, N. Naik, R. Seager, A. C. Clement, and A. van Geen (2003), Warren revisited: Atmospheric freshwater fluxes and "Why is no deep water formed in the North Pacific", *J. Geophys. Res.*, *108*(C6), 3178, doi:10.1029/2001JC001058.

Guo, Z. T., et al. (2001), Origin of the Miocene-Pliocene Red-Earth Formation at Xifeng in northern China and implications for paleoenvironments, *Palaeogeogr. Palaeoclimatol.*

Palaeoecol., *170*, 11–26, doi:10.1016/S0031-0182(01)00235-8.

Hastenrath, S., and L. Greischar (1993), The monsoonal heat budget of the hydrosphere-atmosphere system in the Indian ocean sector, *J. Geophys. Res.*, *98*(C4), 6869–6881, doi:10.1029/92JC02956.

Herbert, T. D., and J. D. Schuffert (1998), Alkenone unsaturation estimates of late Miocene through late Pliocene sea-surface temperatures at Site 958, *Proc. Ocean Drill. Program Sci. Results*, *159T*, 17–21.

Higginson, M. J., et al. (2003), Nitrogen isotope and chlorin paleoproductivity records from the northern South China Sea: Remote vs. local forcing of millennial- and orbital-scale variability, *Mar. Geol.*, *201*(1–3), 223–250, doi:10.1016/S0025-3227(03)00218-4.

Higginson, M. J., et al. (2004), Geochemical evidence for abrupt changes in relative strength of the Arabian monsoons during a stadial/interstadial climate transition, *Geochim. Cosmochim. Acta*, *68*(19), 3807–3826, doi:10.1016/j.gca.2004.03.015.

Honjo, S., et al. (1999), Monsoon-controlled export fluxes to the interior of the Arabian Sea, *Deep Sea Res., Part II*, *46*, 1859–1902, doi:10.1016/S0967-0645(99)00047-8.

Hu, C., et al. (2008), Quantification of Holocene Asian monsoon rainfall from spatially separated cave records, *Earth Planet. Sci. Lett.*, *266*, 221–232, doi:10.1016/j.epsl.2007.10.015.

Hu, J., et al. (2002), Biological markers and their carbon isotopes as an approach to the paleoenvironmental reconstruction of Nansha area, South China Sea, during the last 30 ka, *Org. Geochem.*, *33*(10), 1197–1204, doi:10.1016/S0146-6380(02)00082-7.

Imbrie, J., et al. (1984), The orbital theory of Pleistocene climate: Support from a revised chronology of the marine $\delta^{18}O$ record, in *Milankovitch and Climate, Part 1*, edited by A. L. Berger et al., pp. 269–305, D. Riedel, Hingham, Mass.

Kutzbach, J. E., and P. J. Guetter (1986), The influence of changing orbital parameters and surface boundary conditions on climate simulations for the past 18,000 years, *J. Atmos. Sci.*, *43*(16), 1726–1759, doi:10.1175/1520-0469(1986)043<1726:TIOCOP>2.0.CO;2.

Kutzbach, J. E., X. Liu, Z. Liu, and G. Chen (2007), Simulation of the evolutionary response of global summer monsoons to orbital forcing over the last 280,000 years, *Clim. Dyn.*, *30*, 567–579, doi:10.1007/s00382-007-0308-z.

Laskar, J., et al. (1993), Orbital, precessional, and insolation quantities for the Earth from −20 Myr to +10 Myr, *Astron. Astrophys.*, *270*, 522–533.

Lawrence, K. T., et al. (2006), Evolution of the eastern tropical Pacific through Plio-Pleistocene glaciation, *Science*, *312*, 79–83, doi:10.1126/science.1120395.

Lea, D. W., et al. (2002), Reconstructing a 350 ky history of sea level using planktonic Mg/Ca and oxygen isotope records from a Cocos Ridge core, *Quat. Sci. Rev.*, *21*, 283–293, doi:10.1016/S0277-3791(01)00081-6.

Leuschner, D. C., and F. Sirocko (2003), Orbital insolation forcing of the Indian Monsoon-A motor for global climate changes?, *Palaeogeogr. Palaeoclimatol. Palaeoecol.*, *3111*, 1–13.

Lin, H.-L., et al. (1999), Late Pleistocene nutrients and sea surface productivity in the South China Sea: A record of teleconnections with Northern Hemisphere events, *Mar. Geol.*, *156*, 197–210, doi:10.1016/S0025-3227(98)00179-0.

Lisiecki, L., and M. Raymo (2005), A Pliocene-Pleistocene stack of 57 globally distributed benthic δ^{18}O records, *Paleoceanography*, *20*, PA1003, doi:10.1029/2004PA001071.

Lisiecki, L. E., and M. E. Raymo (2007), Plio-Pleistocene climate evolution: Trends and transitions in glacial cycle dynamics, *Quat. Sci. Rev.*, *26*(1–2), 56, doi:10.1016/j.quascirev.2006.09.005.

Liu, T., and W. Tang (2004), Oceanic influence on the precipitation in India and China as observed by REMM and QuikSCAT, paper presented at 2nd TRMM International Science Conference, Jpn. Aerosp. Explor. Agency, Tokyo.

Liu, T. W., et al. (1994), Evaporation and solar irradiance as regulators of sea surface temperature in annual and interannual changes, *J. Geophys. Res.*, *99*, 12,623–12,637.

Liu, X., et al. (2006), Hemispheric insolation forcing of the Indian Ocean and Asian Monsoon: Local versus remote impacts, *J. Clim.*, *19*, 6195–6208, doi:10.1175/JCLI3965.1.

Liu, X., et al. (2007), A coupled model study of glacial Asian monsoon variability and the Indian Ocean dipole, *J. Meteorol. Soc. Jpn.*, *85*, 1–10, doi:10.2151/jmsj.85.1.

Masson, V., et al. (2000), Simulation of intense monsoons under glacial conditions, *Geophys. Res. Lett.*, *27*, 1747–1750, doi:10.1029/1999GL006070.

McDermott, F. (2004), Palaeo-climate reconstruction from stable isotope variations in speleothems: A review, *Quat. Sci. Rev.*, *23*, 901–918, doi:10.1016/j.quascirev.2003.06.021.

Meehl, G. A. (1997), The south Asian monsoon and the tropospheric biennial oscillation, *J. Clim.*, *10*, 1921–1943, doi:10.1175/1520-0442(1997)010<1921:TSAMAT>2.0.CO;2.

Morley, J. J., and L. E. Heusser (1997), Role of orbital forcing in east Asian monsoon climates during the last 350 kyr: Evidence from terrestrial and marine climate proxies from core RC14-99, *Paleoceanography*, *12*, 483–494, doi:10.1029/97PA00213.

Murray, D. W., et al. (1995), Biogenic sedimentation at Site 847, eastern equatorial Pacific Ocean, during the past 3 M.Y., *Proc. Ocean Drill. Program Sci. Results*, *138*, 429–459.

Murray, R. W., et al. (2000), Analysis of major and trace elements in rocks, sediments, and interstitial waters by inductively coupled plasma-atomic emission spectrometry (ICP-AES), technical note, Ocean Drill. Program, Texas A&M Univ., College Station, Tex.

Pelejero, C., et al. (1999), Molecular biomarker record of sea surface temperature and climatic change in the South China Sea during the last 140,000 years, *Mar. Geol.*, *156*, 109–122, doi:10.1016/S0025-3227(98)00175-3.

Prell, W. L., and J. E. Kutzbach (1992), Sensitivity of the Indian monsoon to forcing parameters and implications for its evolution, *Nature*, *360*, 647–652, doi:10.1038/360647a0.

Qu, T., Y. Du, J. Gan, and D. Wang (2007), Mean seasonal cycle of isothermal depth in the South China Sea, *J. Geophys. Res.*, *112*, C02020, doi:10.1029/2006JC003583.

Raymo, M. E., et al. (2006), Plio-Pleistocene ice volume, Antarctic climate, and the global δ^{18}O record, *Science*, *313*, 492–495, doi:10.1126/science.1123296.

Reichart, G. J., et al. (1998), Temporal variability in the northern Arabian Sea oxygen minimum zone (OMZ) during the last 225,000 years, *Paleoceanography*, *13*, 607–621, doi:10.1029/98PA02203.

Schmiedl, G., and D. C. Leuschner (2005), Oxygenation changes in the deep western Arabian Sea during the last 190,000 years: Productivity versus deepwater circulation, *Paleoceanography*, *20*, PA2008, doi:10.1029/2004PA001044.

Shackleton, N. J., et al. (1984), Oxygen isotope calibration of the onset of ice rafting and history of glaciation in the North Atlantic region, *Nature*, *307*, 620–623, doi:10.1038/307620a0.

Simmonds, I., et al. (1999), Atmospheric water vapor flux and its association with rainfall over China in summer, *J. Clim.*, *12*, 1353–1367, doi:10.1175/1520-0442(1999)012<1353:AWVFAI>2.0.CO;2.

Sun, J., et al. (2001), Spatial and temporal characteristics of dust storms in China and its surrounding regions, 1960–1999: Relations to source area and climate, *J. Geophys. Res.*, *106*(D10), 10,325–10,333.

Sun, Y., et al. (2006), Astronomical timescale and palaeoclimatic implication of stacked 3.6-Myr monsoon records from the Chinese Loess Plateau, *Quat. Sci. Rev.*, *25*, 33–48, doi:10.1016/j.quascirev.2005.07.005.

Tan, S., and G. Shi (2006), Satellite-derived primary productivity and its spatial and temporal variability in the China seas, *J. Geogr. Sci.*, *16*(4), 447, doi:10.1007/s11442-006-0408-4.

Taylor, S. R., and S. M. McClennan (1985), *The Continental Crust: Its Composition and Evolution*, 312 pp., Blackwell Sci, Cambridge, Mass.

Thunell, R., et al. (1999), Sea-surface temperature anomalies associated with the 1997–1998 El Nino recorded in the oxygen isotopic composition of planktonic foraminifera, *Geology*, *27*, 843–846, doi:10.1130/0091-7613(1999)027<0843:SSTAAW>2.3.CO;2.

Tian, J., P. Wang, R. Chen, and X. Cheng (2005), Quaternary upper ocean thermal gradient variations in the South China Sea: Implications for east Asian monsoon climate, *Paleoceanography*, *20*, PA4007, doi:10.1029/2004PA001115.

Tian, J., et al. (2006), Late Pliocene monsoon linkage in the tropical South China Sea, *Earth Planet. Sci. Lett.*, *252*(1–2), 72, doi:10.1016/j.epsl.2006.09.028.

Wajsowicz, R. C., and P. S. Schopf (2001), Oceanic influences on the seasonal cycle in evaporation over the Indian Ocean, *J. Clim.*, *14*, 1199–1266, doi:10.1175/1520-0442(2001)014<1199:OIOTSC>2.0.CO;2.

Wan, S., et al. (2006), Development of the east Asian summer monsoon: Evidence from the sediment record in the South China Sea since 8.5 Ma, *Palaeogeogr. Palaeoclimatol. Palaeoecol.*, *241*(1), 139, doi:10.1016/j.palaeo.2006.06.013.

Wang, B., et al. (2003), Contrasting the Indian and east Asian monsoons: Implications on geologic timescales, *Mar. Geol.*, *201*(1–3), 5–21, doi:10.1016/S0025-3227(03)00196-8.

Wang, L., et al. (1999), East Asian monsoon climate during the Late Pleistocene: High-resolution sediment records from the South China Sea, *Mar. Geol.*, *156*(1–4), 245–284, doi:10.1016/S0025-3227(98)00182-0.

Wang, P. (1999), Response of western Pacific marginal seas to glacial cycles: Paleoceanographic and sedimentological features, *Mar. Geol.*, *156*, 5–40, doi:10.1016/S0025-3227(98)00172-8.

Wang, P., et al. (2005), Evolution and variability of the Asian monsoon system: State of the art and outstanding issues, *Quat. Sci. Rev.*, *24*(5–6), 595, doi:10.1016/j.quascirev.2004.10.002.

Wang, Y. J., et al. (2001), A high-resolution absolute-dated Late Pleistocene monsoon record from Hulu Cave, China, *Science*, *294*, 2345–2348, doi:10.1126/science.1064618.

Wang, Y., et al. (2008), Millennial- and orbital-scale changes in the east Asian monsoon over the past 224,000 years, *Nature*, *451*, 1090–1093, doi:10.1038/nature06692.

Webster, P. J. (1987a), *The Elementary Monsoon*, pp. 3–32, John Wiley, New York.

Webster, P. J. (1987b), The variable and interactive monsoon, in *Monsoons*, edited by J. Fein and P. Stephens, pp. 269–330, John Wiley, New York.

Webster, P. J. (1994), The role of hydrological processes in ocean-atmosphere interactions, *Rev. Geophys.*, *32*, 427–476, doi:10.1029/94RG01873.

Webster, P. J. (2006), The coupled monsoon system, in *The Asian Monsoon*, edited by B. Wang, pp. 1–66, Springer, New York.

Wehausen, R., and H.-J. Brumsack (2002), Astronomical forcing of the east Asian monsoon mirrored by the composition of Pliocene South China Sea sediments, *Earth Planet. Sci. Lett.*, *201*(3–4), 621–636, doi:10.1016/S0012-821X(02)00746-X.

Wei, G., et al. (2003), High-resolution elemental records from the South China Sea and their paleoproductivity implications, *Paleoceanography*, *18*(2), 1054, doi:10.1029/2002PA000826.

Xiao, J., et al. (1995), Grain size of quartz as an indicator of winter monsoon strength on the Loess Plateau of central China during the last 130,000 yr, *Quat. Res.*, *43*, 22–29, doi:10.1006/qres.1995.1003.

Zhu, Y., and R. E. Newell (1998), A proposed algorithm for moisture fluxes from atmospheric rivers, *Mon. Weather Rev.*, *126*, 725–735, doi:10.1175/1520-0493(1998)126<0725:APAFMF>2.0.CO;2.

───────────
G. Chen and Y. Sun, Institute of Earth Environment, Chinese Academy of Sciences, Xi'an 710075, China.

S. C. Clemens and W. L. Prell, Department of Geological Sciences, Brown University, Providence, RI 02912, USA. (steven_clemens@brown.edu)

Z. Liu, Center for Climatic Research, University of Wisconsin, Madison, WI 53706, USA.